Photon detection at subwavelength scales

Wang, Q.

Chapter 3

Position-Dependent Detection Efficiency of a Single NbN Nanowire SSPD

We probe the local detection efficiency in a nanowire superconducting single-photon detector along the cross section of the wire with a spatial resolution of 10 nm. We find a strong variation in the local detection efficiency of the device. Our experimental results agree with theoretical calculations based on a photon-assisted vortex entry model[1].

3.1 Introduction

Nanowire superconducting single-photon detectors (SSPDs) consist of a superconducting wire of nanoscale cross section [14], typically 5 nm by 100 nm. Photon detection occurs when a single quantum of light is absorbed and triggers a transition from the superconducting to the normal state. SSPDs have high efficiency, low jitter, low dark count rate and fast reset time [61], and are therefore a key technology for, among others, quantum key distribution [50], interplanetary communication [62] and cancer research [63].

Although considerable progress has been made recently, the underlying physical mechanism responsible for photon detection on the nanoscale is still under active investigation. A combination of theory [23, 60], experiments [30,

[1]This chapter is based on J. J. Renema, Q. Wang, R. Gaudio, I. Komen, K. op't Hoog, D. Sahin, A. Schilling, M. P. van Exter, A. Fiore, A. Engel, and M. J. A. de Dood, Nano Lett. **15**, 4541, (2015).

38,40], and simulations [24,25] on NbN SSPDs indicates that the absorption of a photon destroys Cooper pairs in the superconductor and creates a localized cloud of quasiparticles that modifies the current distribution in the wire. This, in turn, can make the wire susceptible to the entry of a magnetic vortex from the edge of the wire by lowering the energy barrier for vortex entry; this barrier depends on the superconducting electron density near the edge of the wire. A photon being absorbed near the edge generates a substantial decrease in this density near that edge and thus a quite large decrease in the energy barrier for vortex entry. Contrarily, when a photon is absorbed in the middle of the wire, the superconducting electron density decrease near the edge is small and the energy barrier for vortex entry is only little affected by the absorption of the photon. Energy dissipation by the vortex moving across the wire drives the system to the normal state and causes the detector to "click". The "click" probability thus depends on the location of the photon-absorption within the wire (edge or center). An important implication of this detection model is that such a detector has non-uniform detection probability with photons absorbed close to the edge having a higher local detection efficiency compared to photons absorbed in the center of the wire [25].

This effect has practical implications for the operation of SSPDs, since it represents a potential limitation on the detection efficiency [42]. In addition, SSPDs have been proposed for nanoscale sensing, either in a near-field optical microscope configuration [32] or as a subwavelength multiphoton probe [64], where this effect would be of major importance for the properties of such a microscope. While this effect has been predicted theoretically, clear experimental evidence is missing.

In this chapter, we experimentally explore the nanoscale variations in the intrinsic response of the detector. We explore the spatial variations in the detection efficiency with a resolution of approximately 10 nm, i.e., better than $\lambda/50$, using far-field illumination only. We find that our results are qualitatively consistent with numerical simulations [24,25].

The key technique used in this work is a differential polarization measurement that probes the internal detection efficiency of the detector. The technique is based on the fact that polarized light is preferentially absorbed at different positions for the two orthogonal polarizations, due to differences in boundary conditions. Using this technique, we achieve selective illumination of either the edges or the middle of the wire. By doing so at different wavelengths, we are able to probe the intrinsic photodetection properties of our device on the nanoscale.

3.2 Separation of optical absorption and internal detection efficiency

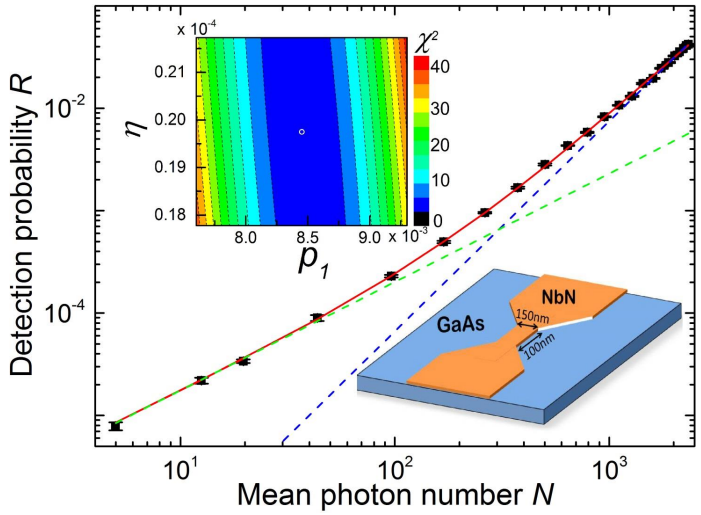

Figure 3.1: Detection probability as a function of input photon number at a wavelength of 1500 nm. The points represent experimental data with error bar. The red curve represents the fit by quantum detector tomography. The data are shown for a bias current equal to $I_b = 22.7\ \mu$A; we find that $\eta = 1.98\times10^{-4}$ and $p_1 = 8.46\times10^{-3}$. The top inset provides a landscape picture of how the reduced χ^2 varies with η and p_1, and the white circle indicates the minimum of χ^2. The bottom inset shows the structure of the SSPD, in which a single NbN nanowire is patterned in between two broader parts on a GaAs substrate, and an 80 nm thick HSQ layer (not shown) is covered on the NbN nanowire.

It is well known that changing the polarization of the incident light results in a change in overall optical absorption in an anisotropic structure such as a wire or a meander [42, 47, 65–67]. Therefore, our first task is to separate the probability that a photon is absorbed from the internal detection efficiency, where the latter is defined as the conditional probability that an absorbed photon causes a detection event. To make this separation, we use quantum detector tomography (QDT) [28–30, 34, 36–38, 53, 68–70].

QDT records the detector response to a set of known quantum states of light and distills from these measurements the detection probability for different photon numbers for the detector as a whole. As shown in Chapter 2 and Ref. [29], this procedure allows us to unambiguously separate the single-photon detection probability p_1 from the probability η that a photon is absorbed. We find that η is almost independent of detector bias current for a nano SSPD and that its value is consistent with the geometric area of the detector [29]. Hence,

we identify p_1 with the internal detection efficiency conditional on photon absorption, which we henceforth refer to as the internal detection efficiency or IDE.

Figure 3.1 shows, on a log-log scale, the measured detection probability R (points) as a function of mean photon number N for an illumination wavelength of 1500 nm. The data have been taken at a detector bias current of $I_b = 22.7$ μA ($I_b/I_c = 0.81$, where I_c is the device critical current). The bottom right inset shows the schematic structure of the SSPD in the experiment. A 150 nm wide, 100 nm long and 5 nm thick nanowire in between two tapered parts is fabricated on a semi-infinite GaAs substrate. The NbN is deposited on the GaAs substrate which is subsequently patterned by e-beam lithography and reactive ion etching [27], leaving an 80 nm thick HSQ (Hydrogen silsesquioxane) layer on top of the NbN nanowire for protection. The line through the data corresponds to the result of our QDT analysis. From the fit we find an internal detection efficiency $p_1 = 8.46 \pm 0.17 \times 10^{-3}$, $p_2 = 4.02 \pm 0.08 \times 10^{-1}$, and an absorption efficiency $\eta = 1.98 \pm 0.04 \times 10^{-4}$. We note that the small value of η is related to the ratio between the active area of the nanodetector and the area of the optical beam. This ratio is small because the beam size was kept large to become insensitive to small variations in optical alignment. The two dashed lines in Fig. 3.1 indicate detection in the one-photon regime (green) and in the two-photon regime (blue), displaying a clear distinction between the two regimes.

Linear independence of fit parameters is illustrated in the top left inset, which shows a false color plot of the reduced goodness-of-fit χ^2 as a function of η and p_1. The white circle shows the minimum value of the reduced χ^2, which represents the best fit. As can be seen in the inset, p_1 and η can be determined with high accuracy (more details in Chapter 2).

3.3 Polarization-dependent internal detection efficiency

We have repeated the QDT procedure for different input polarizations and wavelengths of the incident light. Figure 3.2(a) shows the IDE and effective absorption efficiency η as a function of polarization at a wavelength of 1500 nm. The error bars in the figures are calculated from the standard deviation of a series of independent experiments. Note that the parameters obtained from this QDT analysis are quantities that represent the detector as a whole. A simple model of the detector would assume that only the effective absorption efficiency η depends on the polarization of the incident light.

So, it comes as a surprise that Fig. 3.2(a) shows that not only η but also the IDE is polarization dependent; actually they oscillate in phase as a function

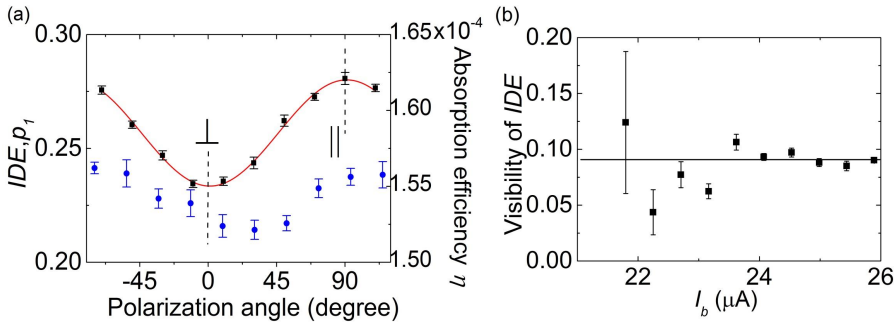

Figure 3.2: Polarization dependence of the internal detection efficiency at a wavelength of 1500 nm. (a) shows the internal detection efficiency IDE or p_1 (black squares) and the effective absorption efficiency η (blue dots) as a function of the polarization of the incident light. The internal detection efficiency points are fitted by a sine function (red curve). The minimum and maximum of the fit are noted as perpendicular $\perp$ and parallel $\parallel$. (b) shows polarization visibility of the IDE as a function of bias current. The horizontal curve represents the current averaged visibility.

of the polarization direction relative to the nanowire. We therefore introduce the visibility of the IDE as

$$V_{IDE} = (p_{1,max} - p_{1,min})/(p_{1,max} + p_{1,min}). \tag{3.1}$$

To verify that our observation of a polarization-dependent IDE is robust we repeated the experiment for different bias currents. We find that the values of p_i depend strongly on bias current, as expected [38]. The visibility V_{IDE}, however, is independent of bias current and has an average value of 0.09 for the wavelength of 1500 nm, which is represented by the horizontal line in Fig. 3.2(b). Furthermore, we observe that the maximal and minimal IDE ($p_{1,max}$ and $p_{1,min}$) occur when the polarization is parallel and perpendicular to the nanowire, respectively. This indicates that under perpendicular illumination the absorbed photon is less likely to cause a detection event.

To find a physical explanation of the observed polarization dependence the simple model that we have used so far needs to be extended. While the QDT analysis yields an effective absorption efficiency η, it is well known that the optical absorption is position dependent, because of different boundary conditions for electric fields parallel and perpendicular to the nanowire. A possible interpretation of the polarization-dependent IDE is thus to assume that the observed internal detection efficiency itself depends on position. Therefore, we introduce a new quantity, namely the local detection efficiency $LDE(x)$ to take these spatial variations into account. The observed polarization dependence is a combination of the position-dependent absorption distribution $A(x)$ and a position-dependent local detection efficiency $LDE(x)$, where the latter can

be interpreted as the conditional probability that the detector produces a click given that a photon is absorbed at position x.

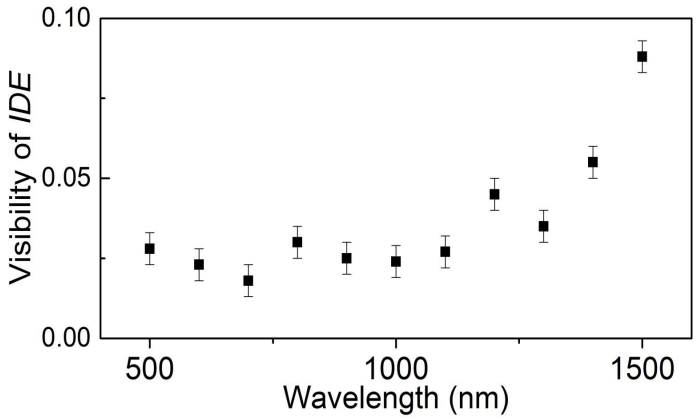

Figure 3.3: Plot of the visibility of the internal detection efficiency. For each wavelength the current-averaged value of the visibility is displayed.

Both the absorption efficiency and the local detection efficiency depend on wavelength. A description of the polarization and wavelength dependent IDE as measured by QDT is then given by:

$$IDE_k(\lambda) = \frac{\int A_k(\lambda, x) LDE(\lambda, x) dx}{\int A_k(\lambda, x) dx}, \tag{3.2}$$

where λ is the wavelength of illumination, and the subscript $k = \{\|, \perp\}$ refers to the polarization. The optical absorption distribution $A_k(\lambda, x)$ can be obtained by numerically solving Maxwell's equations (see Section 3.4), and the $LDE(\lambda, x)$ can be considered as fitting parameters, in which x is the variable and λ is a well described constraint (see Section 3.5).

We have measured the visibility V_{IDE} of the internal detection efficiency at a large wavelength range from 400 nm to 1500 nm. Figure 3.3 shows the measured visibility V_{IDE} as a function of wavelength. As a result, $LDE(\lambda, x)$ at a particular wavelength can be determined by the fit. The results of $LDE(x)$ and details of the fit are introduced in the following sections.

3.4 Optical absorption

Before discussing the local detection efficiency $LDE(\lambda, x)$ we report on the calculated absorption distribution $A(\lambda, x)$. The aim of this section is to reduce the complexity of the problem by replacing the 3D absorption with an approximate 2D calculation of $A(\lambda, x)$ that only depends on the transverse coordinate x.

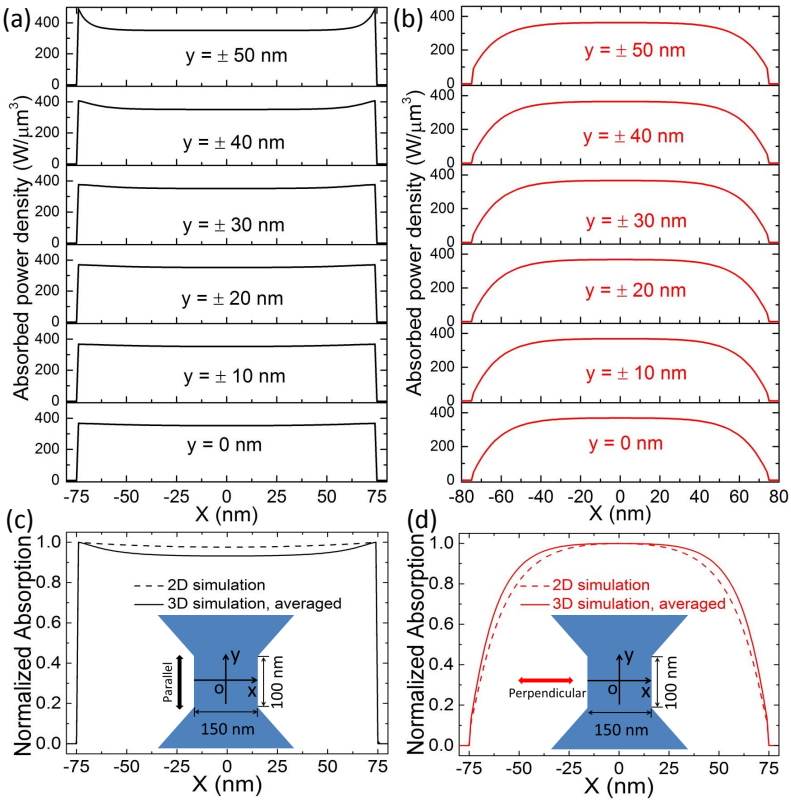

Figure 3.4: Absorption distribution by FDTD simulation at the wavelength of 1500 nm for parallel (left) and perpendicular (right) polarization. For each polarization, (a) and (b) obtained from 3D simulation show the absorption density across the wire (x-direction) at different y positions from the center ($y = 0$ nm) to the ends ($y = \pm$ 50 nm) of the nanowire. (c) and (d) compare the 3D absorption density averaged on y position (solid line) and 2D absorption density (dashed line).

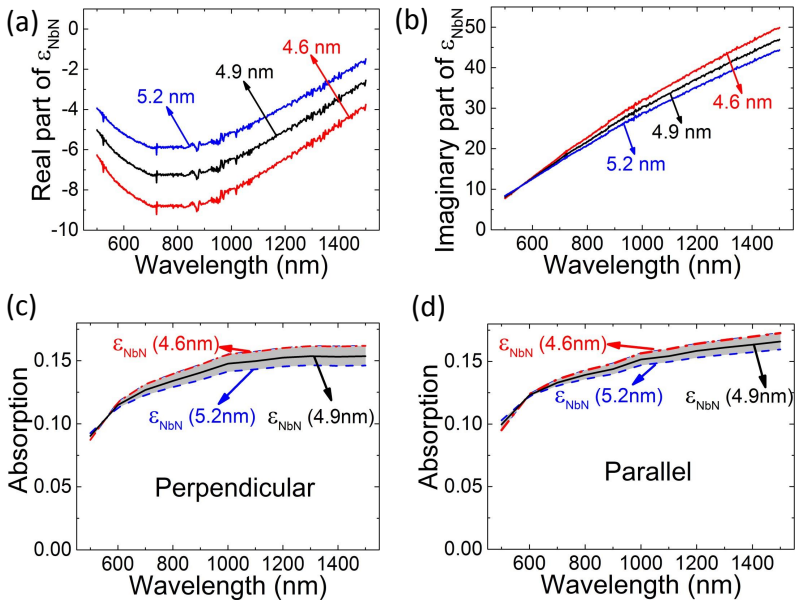

Figure 3.5: Dielectric constant of our NbN film as obtained by ellipsometry by assuming different values for the film thickness. (a) and (b) show the real and imaginary part of the dielectric constant. (c) and (d) show calculated absorption spectra for parallel and perpendicular polarization using the value of the dielectric constant shown in (a) and (b).

The absorption in the NbN nanowire is calculated using a commercial finite-difference-time-domain method (FDTD, FullWave package, RSoft [71]). We take a 3D simulation at a wavelength of 1500 nm for example. In the simulation, we describe the materials as shown in Fig. 3.1 (with an 80 nm layer of HSQ on top of NbN nanowire). Figures 3.4(a) and 3.4(b) show the 1D absorption distribution across the nanowire from center ($y = 0$ nm) to the boundaries between the nanowire and the tapered parts ($y = \pm$ 50 nm) obtained from the 3D simulations. For both parallel and perpendicular illumination, the absorption profiles do not depend much on the coordinate y, which demonstrates that the tapered parts have minimal influence on the absorption of the nanowire. This allows us to perform a simpler and more efficient 2D simulation of the cross section of the nanowire to describe the absorption distribution in the nanowire.

Figures 3.4(c) and 3.4(d) show the comparison of simulations for a 2D infinite wire (dashed) and the 3D geometry (solid). The 3D absorption curve is obtained by averaging the absorption curves at different y positions in Figs. 3.4(a) and 3.4(b). The absorption curves from 2D and 3D simulations are normalized to their maximum because we are interested in the relative difference between the curves. We find that in case of perpendicular illumination the absorption mainly occurs in the middle of the nanowire while for the parallel case the absorption is roughly uniform over the entire nanowire. There is very little difference between 2D and 3D simulations for both parallel and perpendicular illumination in our geometry, justifying the use of much more efficient 2D simulations for other wavelengths.

The optical absorption is determined by the dielectric constant of NbN, which is obtained via ellipsometry [72]. In Ref. [72] a thickness of 4.9 nm was estimated. We assume a conservative error bar of 0.3 nm on the thickness, and recalculate epsilon via numerical inversion of the ellipsometry data for three different thicknesses resulting in the curves shown in Figs. 3.5(a) and 3.5(b).

Based on the three sets of the dielectric constant we calculate the absorption for perpendicular and parallel illumination, which are shown in Figs. 3.5(c) and 3.5(d). For most wavelengths (600 nm –1500 nm), the film absorbs most if we assume the film to be thinnest (4.6 nm), which is due to the larger imaginary part of the dielectric constant. The variations in the dielectric constant are treated as systematic error in the following sections.

3.5 Position-dependent local detection efficiency

In order to distill from Eq. (3.2) the local detection efficiency $LDE(\lambda, x)$ a relation between wavelength (photon energy) and local detection efficiency is needed. This allows inversion of Eq. (3.2) to find $LDE(\lambda, x)$ given the measured

$IDE(\lambda)$ as a function of wavelength. Our experimental work in SSPDs [30,38] shows that the photon-detection probability depends exponentially on bias current, and that a linear relation exists between photon energy and bias current for a certain internal detection efficiency [25,38]. Based on these observations we postulate a similar bias current dependence of the microscopic $LDE(\lambda, x)$:

$$LDE(\lambda, x) = \min\{1, \exp[(I_b - I_{th}(\lambda, x))/I^*]\}, \tag{3.3}$$

with a threshold current defined as

$$I_{th}(\lambda, x) = I_c - \gamma'(x)\frac{hc}{\lambda}. \tag{3.4}$$

Here hc/λ is the photon energy and $I^* = 0.65$ μA is an experimentally determined current scale for our detector [38]. $\gamma'(x)$ is the local energy-current interchange ratio, which parameterizes the internal detection efficiency of the nanowire at different excitation wavelengths, and translates to a threshold current $I_{th}(\lambda, x)$ that is sufficient to quantify this local internal efficiency [25]: when the bias current I_b exceeds $I_{th}(\lambda, x)$ with a photon absorbed at position of x, the energy barrier for a vortex vanishes, leading to the entry of the vortex and to a detection event.

In practice, instead of using $LDE(\lambda, x)$ for fitting the measured visibility V_{IDE} we employ $\gamma'(x)$ as fitting parameter. The outcome should be comparable to the detailed calculation based on quasiparticle-diffusion and vortex-crossing, as introduced in Appendix I.

Figure 3.6 shows the measured visibility V_{IDE} as a function of wavelength (squares), a best fit (red), a fit with a constraint (green) and the results of a calculation using the function $\gamma'(x)$ predicted by numerical modeling of the detection process. The details of the fit procedure are given in Appendix II. The original fit (red) is based on Eqns. (3.2) and (3.3) as discussed above with fitting parameters $\gamma'(x)$ at discrete positions x. Mirror symmetry of $\gamma'(x)$ and a parametrization with 9 points is sufficient to capture all details observed in the experiment. The results for $I_{th}(x)$ at $\lambda = 1500$ nm derived from the fitted values of $\gamma'(x)$ are shown in Fig. 3.7(a), the curve (red) contains a distinct minimum at $x = \pm$ 40 nm.

To verify whether these minima are robust we constrain $\gamma'(x)$ to monotonically vary from the center of the nanowire to the edge. In Fig. 3.7(a), the green curve shows the variation in $I_{th}(x)$ under these constraints. However, Fig. 3.6 shows that the visibility (green) is only marginally affected by constraining $\gamma'(x)$. This analysis suggests that the spatial variations in the threshold current close to the edge can not be extracted in great detail.

A different point is how our results compare with theory. This comparison is shown both in Figs. 3.6 and 3.7(a), where the blue curves represent the

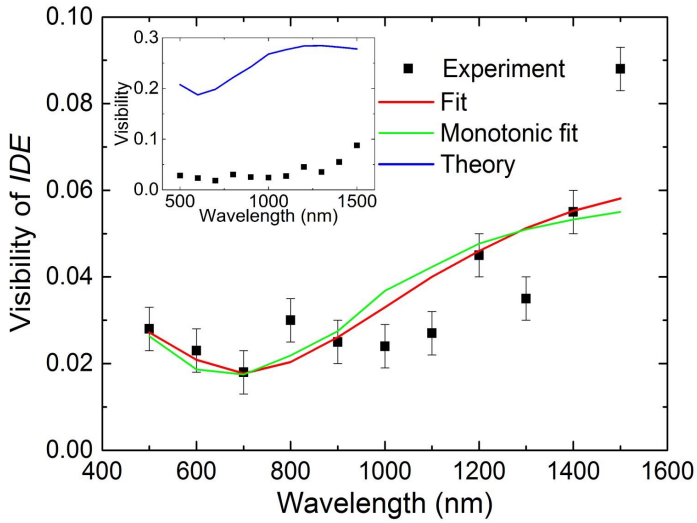

Figure 3.6: Visibility of internal detection efficiency and fit. For each wavelength the visibility is averaged from all the currents. The red curve is the fit by considering the distribution of absorption and internal detection efficiency, and the green curve is the fit by considering a constraint to make the variance of local detection efficiency monotonic from the center of the nanowire to the edge. The blue curve in the inset shows the visibility calculated based on the photon detection theory [25].

predictions by the numerical model of the detector. We find that the visibility is a factor of 10 larger (inset of Fig. 3.6), and that the threshold current from the numerical calculation has a notably stronger edge/center contrast (Fig. 3.7)(a).

The comparison of the results from experiment and numerical modeling brings up the following question: "Is there a link between the wavelength averaged value of the V_{IDE} and the width of the main feature of the threshold current $I_{th}(x)$ as shown in Fig. 3.7(a)?"

To answer this question we determine $I_{th}(x)$ for various values of V_{IDE} assumed to be wavelength independent, with $0.03 < V_{IDE} < 0.3$. The results are shown in Fig. 3.7(b), in support of our conjecture that a broader profile of $I_{th}(x)$ leads to a sharper contrast between the edge and the center of the nanowire, and to a larger visibility consequently.

Finally, in Fig. 3.7(c) we show, using the results of Fig. 3.7(a) how the $LDE(x)$ varies with the location of the photon absorption. The results are shown based on both the experimental data (solid, red) and the numerical calculations (dashed, blue), for different values of the bias current. Note that the relatively small spatial variations in the $I_{th}(x)$ translate in much larger variations in $LDE(x)$, up to factors 10 – 20. Also note that the detector saturates at the edges before saturating at the center.

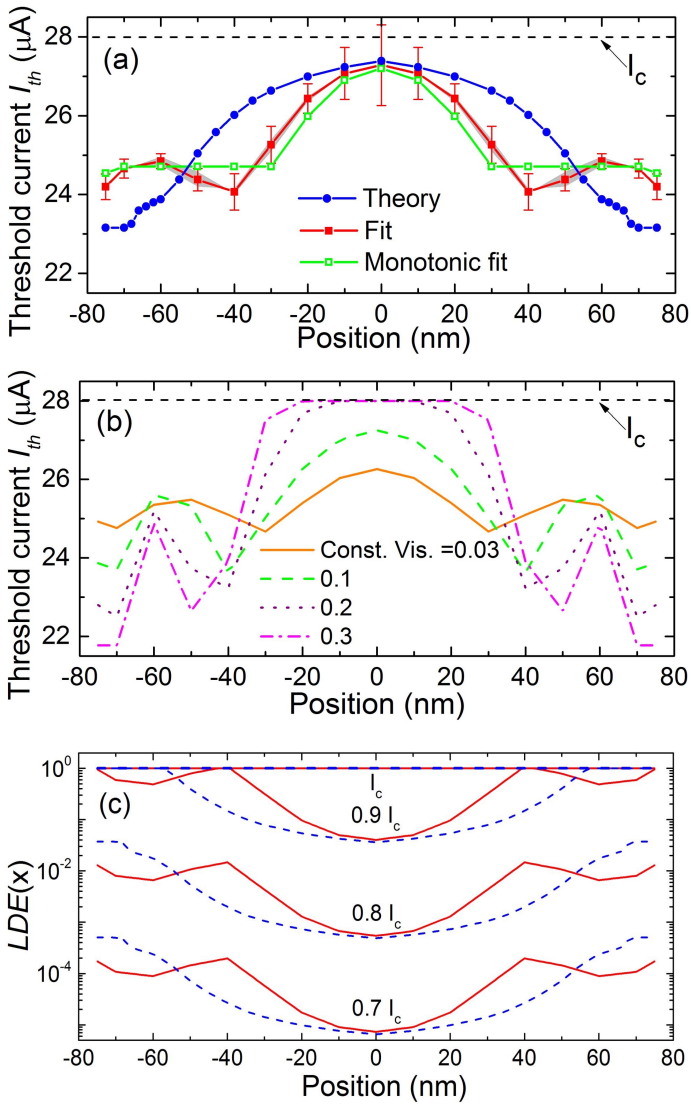

Figure 3.7: Threshold current and local detection efficiency at wavelength of 1500 nm. (a) shows the threshold current obtained from experiments (open and closed squares) and theory (dots). The grey area on the solid curve indicates the systematic error from calculation of optical absorption. The monotonic fit is obtained by using a constraint to make the fitting parameters monotonic from the center of the nanowire to the edge. (b) shows the threshold current by fitting a set of constant visibility from 0.03 to 0.3. (c) shows the local detection efficiency based on (a) : solid lines from experiment and dashed lines from theory.

3.6 Conclusions

We have separated the polarization-dependent internal detection efficiency from the optical absorption of an SSPD via quantum detector tomography. The internal detection efficiency is constructed by the optical absorption and position-dependent local detection efficiency, which depends on the position along the cross section at which the photon is absorbed. We have probed this effect with a resolution of approximately 10 nm, and found agreement with theoretical calculations done in the context of the quasiparticle-diffusion-based vortex-crossing model. Compared to the theory, we have confirmed that a narrower profile of threshold current is able to fit the experimental data. Within a range of $\sim$ 30 nm close to the edge of the nanowire the local detection efficiency is much higher than at the center, which is relevant to the scale of the quasiparticle diffusion after photon absorption. These experimental conclusions support the model of quasiparticle diffusion and vortex entry, and quantitatively describe the photon-detection process in the NbN nanowire SSPD on the nanoscale.

3.7 Appendix I: Photon detection mechanism

In the main text of Chapter 3, we use a quasiparticle-diffusion and vortex-crossing model to describe the photon detection process in a NbN superconducting single-photon detector. This appendix summarizes the model originally presented in Ref. [24] with a few additions to make the model more realistic. This model assumes that the photon excites one electron with energy hc/λ. The excited electron diffuses in the plane of the film with a diffusion constant D_e, and thermalizes via inelastic scattering with other electrons, Cooper-pairs and the lattice. Neglecting details of this thermalization process, an exponential increase of excess quasiparticles is assumed with a time constant τ_{qp} and an overall efficiency ς [22]. The excess quasiparticles themselves are also subject to diffusion with a temperature-dependent diffusion constant $D_{qp} < D_e$ and eventually recombine to form Cooper-pairs on a time-scale $\tau_r > \tau_{qp}$. The entire process can be described by the following coupled differential equations [24]:

$$\frac{\partial C_e(r,t)}{\partial t} = D_e \nabla^2 C_e(r,t) \tag{A.1}$$

$$\frac{\partial C_{qp}(r,t)}{\partial t} = D_{qp}\nabla^2 C_{qp}(r,t) - C_{qp}/\tau_r + \frac{\varsigma h\nu}{\Delta \tau_{qp}} \exp(-t/\tau_{qp}) C_e(r,t) \tag{A.2}$$

with Δ the superconducting gap, $C_e(r,t)$ the probability density to find the excited electron at position r at time t after photon absorption and $C_{qp}(r,t)$ the quasiparticle density.

An estimation of the Ginzburg-Landau relaxation time results in $\tau_{GL} < 1$ ps. Therefore, we assume the current redistribution due to the spatial variation of the density of superconducting electrons $n_{se} - C_{qp}(r,t)$ to be instantaneous on time scales > 1 ps. To obtain a more realistic current-distribution than in Ref. [24], we now apply the relation that the velocity of superconducting electrons can be calculated from the gradient of the phase of the superconducting condensate [25]:

$$v_S = \frac{\hbar}{m}\nabla\varphi \tag{A.3}$$

with a corresponding current density

$$j_s = -e n_{se} \frac{\hbar}{m}\nabla\varphi \tag{A.4}$$

and the continuity equation that needs to be solved:

$$\nabla \cdot (-e n_{se} \nabla\varphi) = 0, \tag{A.5}$$

where we use the previously calculated quasiparticle distribution to obtain n_{se}. Additionally, we take into account that the density of superconducting electrons depends on the velocity v_s [73].

$$n_{se} \propto 1 - (v_s/v_c)^2/3, \tag{A.6}$$

with v_c the critical velocity at the critical-current density j_c. Thus Eq. (A.5) becomes nonlinear. Once we know the current distribution, the potential energy experienced by a vortex can be calculated as suggested in Ref. [41]. More details about the refined numerical model can be found in Ref. [25].

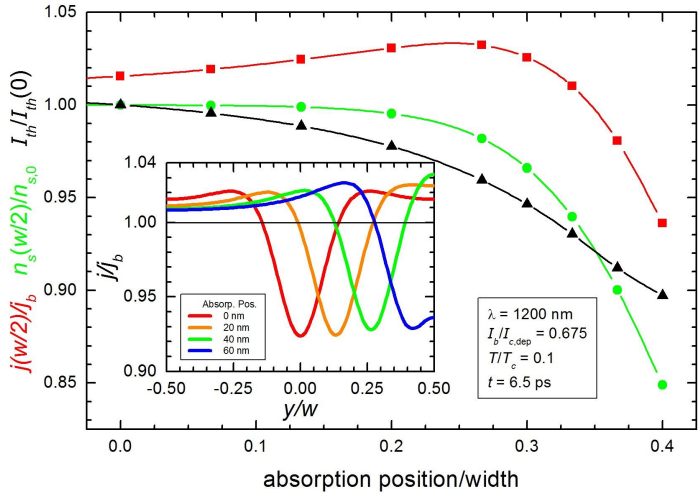

Figure A.1: Variation of reduced current density at the edge $j(w/2)/j_b$, normalized density of superconducting electrons $n_s(w/2)/n_{s,0}$, and rescaled threshold current for photon detection as a function of the distance of the photon absorption position from the center of the wire. The variation of the threshold current near the center of the wire is dominated by the variation of the current density at the edge. For absorption events closer to the edge the reduction of the density of superconducting electrons becomes the dominating effect. In the inset we show the variation of the current density across the wire for different absorption positions.

In the inset of Fig. A.1 we plot reduced current densities j/j_b across the strip for some absorption positions. At first, current densities increase with decreasing distance of the absorption position to the near edge. If the distance becomes less than 20 nm to the edge the current density near the edge is reduced, eventually below the equilibrium bias current density j_b.

In the main graph of Fig. A.1 the reduced current density at the edge $j(w/2)/j_b$ is plotted as a function of absorption position, together with the density of superconducting electrons at the edge $n_s(w/2)$ normalized to their equilibrium

density $n_{s,0}$, and the threshold current scaled by the threshold current for absorption in the center $I_{th}/I_{th}(0)$. For absorption events near the center, the variation of the threshold current is mostly determined by the variation of the current density at the edge, since the density of superconducting electrons at the edge remains approximately constant. At close distances to the edge n_s is significantly reduced at the edge. This is the reason for a reduced current density at the edge, but additionally leads to a reduction of the vortex self-energy which is proportional to n_s. This second effect is stronger than the effect of the reduced current density and as a result we obtain a monotonic reduction of the threshold current for vortex entry as a function of the distance from the strip center.

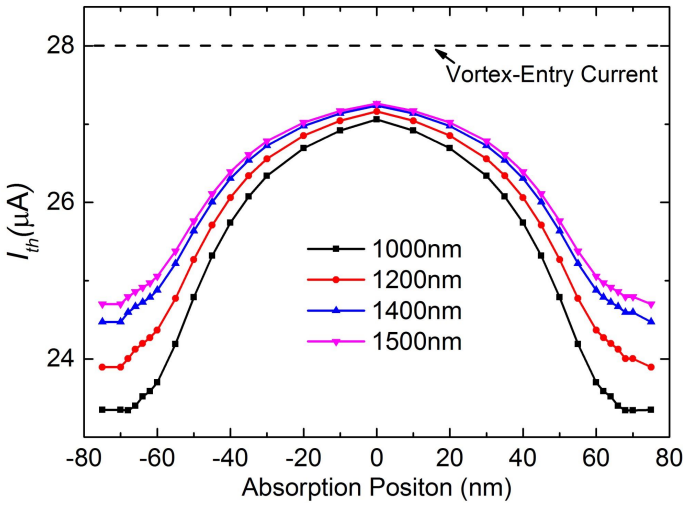

Figure A.2: Calculated threshold current as a function of the distance of the photon absorption position from the center of the wire for different photon wavelengths. The relative reduction of the threshold current for absorption near the edge compared to absorption in the center increases with increasing photon energy for the energy range considered in this study.

We define the threshold current as that value of the bias current for which the maximum potential energy for a vortex becomes zero. In this case we expect an internal detection efficiency equal to one. With this criterion, we obtain the energy dependence of the threshold current as a function of position, which is plotted in Fig. A.2. The vortex-entry current without photon absorption is also indicated by the horizontal line. This curve is symmetric with respect to the center line of the wire due to the symmetry between vortices and antivortices in zero applied magnetic field. There is a significant reduction of the threshold current for photons absorbed near the edge of around 10% as compared to the center of the wire. We would like to point out that for each position in the

wire we find a linear relation between threshold current and photon energy, consistent with previous experimental results [30, 38, 74].

As the photon energy increases and as absorption occurs closer to the edge, the relation between the density of superconducting electrons and the current distribution (Eqns. (A.5) and (A.6)) becomes more nonlinear. For absorptions very close to the edge, the nonlinear solver produces systematic errors. For all wavelengths, we do not calculate the detection current for absorption sites closer than one coherence length ($\xi \approx 4$–5 nm for NbN) to the edge of the wire. For short wavelengths, the area in which this occurs increases, to approximately 12 nm from each edge at 800 nm. In our calculations, we assume that the detection current this close to the edge of the wire is weakly dependent on the absorption position and set it constant, with a value equal to the threshold current in the point closest to the edge that we can still reliably compute. In our experiment, we are operating below this threshold current. To convert the threshold current into a local detection efficiency, we assume a functional dependence of the form $p \equiv IDE = \exp((I_b - I_{th})/I^*)$; where $I^* = 0.65$ μA is an experimentally determined scaling current. In this way, we obtain the variation of the internal detection efficiency for a given bias current as shown in the Fig. 3.7(c) in the main text.

3.8 Appendix II: Fit to visibility

The photon detection mechanism in Appendix I shows that the probability of vortex entry depends on the position of the photon absorption. Hence, we use the position-dependent local detection efficiency $LDE(\lambda, x)$ to quantify the microscopic detection process. We assume that the internal detection efficiency IDE as a function of wavelength can be constructed as follows:

$$IDE_k(\lambda) = \frac{\int A_k(\lambda, x) LDE(\lambda, x) dx}{\int A_k(\lambda, x) dx}, \tag{A.7}$$

where k stands for either parallel or perpendicular polarization, $A_k(\lambda, x)$ is the absorption distribution obtained by FDTD simulation at an incident wavelength of λ, and the $LDE(\lambda, x)$ is the efficiency to trigger the detector for the absorbed photon with energy hc/λ at position x. In the integral, the absorption profile $A_k(x)$ is normalized in order to remove the dependence on average absorption probability $\int A_k(\lambda, x) dx$, because the average absorption (effective absorption efficiency) η is separated from the IDE via quantum detector tomography.

For a certain wavelength, we find that IDE depends exponentially on bias current I_b, which is supported by experiment in this work and a previous study [38]. Therefore we use a microscopic $LDE(\lambda, x)$:

$$LDE(\lambda, x) = \min\{1, \exp[(I_b - I_{th}(\lambda, x))/I^*]\}, \tag{A.8}$$

where $I^* = 0.65$ μA is an experimentally determined current scale.

In order to combine the information from different wavelengths, we posit a relation between photon energy and the threshold current $I_{th}(\lambda, x)$ [25, 30]:

$$I_{th}(\lambda, x) = I_c - \gamma'(x) \frac{hc}{\lambda}, \tag{A.9}$$

where I_c is the critical current, hc/λ is the photon energy, and $\gamma'(x)$ is the local energy-current interchange ratio, which parameterizes the detection probability of the wire at different excitation wavelengths. The assumption is based on the fact of the linear relation of bias current and incident energy of photon.

The assumptions leading to Eqns. (A.8) and (A.9) make it possible to perform a numerically inversion. From the measured wavelength dependence we obtain the parameters $\gamma'(x)$ via fitting the experimental data. We use mirror symmetry about $x = 0$ and 9 points for $\gamma'(x)$. We use the following procedure:

1) The strongly position-dependent $A_k(\lambda, x)$ is calculated with a spatial resolution of 1 nm by FDTD simulation. Therefore, to calculate the integral of Eq. (A.7) we linearly interpolate $\gamma'(x)$ on a 1 nm grid, from the points at which it is given. We assume mirror symmetry around point $x = 0$.

2) For each wavelength, we compute $I_{th}(\lambda, x) = I_0 - \gamma'(x)\frac{hc}{\lambda}$, and take I_0 to be $I_{c,exp} = 28$ μA, in accordance with the theoretical predictions of the vortex-crossing model.

3) For each current and wavelength, we compute the local detection efficiency: $LDE(\lambda, x) = \min\{1, \exp[(I_b - I_{th}(\lambda, x))/I^*]\}$.

4) Compute $IDE_k(\lambda)$ according to Eq. (A.7) and the visibility $V = (IDE_{\|} - IDE_{\perp})/(IDE_{\|} + IDE_{\perp})$.

In order to fit the visibility to the experimental data, we use Tikhonov regularization [75]. That is, to the usual function that is minimized in an inversion problem

$$g(x) = \sum (V_i(\gamma'(x)) - V_{i,exp})^2/\sigma_i^2, \tag{A.10}$$

where $V_{i,exp}$ is the observed visibility and σ is the error on each visibility. We add an extra term, replacing $g(x)$ by

$$g(x) = \sum (V_i(\gamma'(x)) - V_{i,exp})^2/\sigma_i^2 + s\sum (\gamma'(x_j) - \gamma'(x_{j+1}))^2, \tag{A.11}$$

which has the effect of penalizing solutions where the difference between adjacent points in the curve is large. We apply only weak regularization such that the contribution to $g(x)$ from the second term is approximately 20% of the first. Furthermore, we apply the constraint that the sum $\gamma'(x)$ should be equal to the sum of the theoretical $\gamma'(x)$ curve. We find that we can fit our data if we set $\sum \gamma'(x)\Delta x_i = 1.15 \sum \gamma'(x)_{theo}\Delta x_i$. We varied the number of points and value of s and verified that the solution presented in the main text is robust against the small variation in the parameter s.